Boundary-Layer Meteorology (2021) 178:91–118
https://doi.org/10.1007/s10546-020-00561-6

RESEARCH ARTICLE

Nested Large-Eddy Simulations of the Displacement of a Cold-Air Pool by Lee Vortices

Alex Connolly[1] · **Fotini Katopodes Chow**[2] · **Sebastian W. Hoch**[3]

Received: 15 October 2019 / Accepted: 5 August 2020 / Published online: 25 August 2020

Abstract
Mesoscale simulations are typically performed at coarse resolutions that do not adequately represent underlying topography; nesting large-eddy simulations within a mesoscale model can better resolve terrain and hence capture topographically-induced stable flow phenomena. In the case of the Mountain Terrain Atmospheric Modelling and Observations (MATERHORN) program, large temperature fluctuations were observed on the slope of Granite Peak, Utah, which partially encloses a cold-air pool in the east basin. These flow features are able to be resolved using large-eddy simulation within the Weather Research and Forecasting (WRF) model with $\Delta x = 100\,\mathrm{m}$, allowing accurate representation of lee vortices with horizontal length scale of $\mathcal{O}(1\,\mathrm{km})$. At this resolution, terrain slopes become quite steep, and some model warm biases remain in the east basin due to limits on terrain-following coordinates that prevent the model from fully resolving drainage flows with this steep terrain. A new timestep limit for the WRF model related to these steep slopes is proposed. In addition, the initialization of soil moisture is adjusted by drying the shallowest layer to assist the formation of a cold pool in the large-eddy simulation. These real case simulations compare well to observations and also to previously published simulations using idealized configurations to study similar phenomena. For instance, the values of non-dimensional mountain height, which characterize flow regimes in idealized studies, are similar in the real case.

Keywords Cold-air pool · Large-eddy simulation · Lee vortices · Mountain meteorology · Numerical weather prediction

1 Introduction

Stably stratified flows, typical of the nocturnal atmospheric boundary layer, are affected by the presence of complex terrain in ways not seen under neutral or unstable conditions

✉ Alex Connolly
adac@berkeley.edu

[1] Department of Civil and Environmental Engineering, University of California, Berkeley, 205 O'Brien Hall, Berkeley, CA 94720, US

[2] Department of Civil and Environmental Engineering, University of California, Berkeley, CA, US

[3] Department of Atmospheric Science, University of Utah, Salt Lake City, UT, US

(Baines 1998). In large part, this is due to the decoupling of synoptic flows and low-level flows within a near-surface inversion, which inhibits vertical mixing of momentum from aloft. Flow blocking and channeling also play major roles when air parcels are too dense to rise up and over obstacles (Chow et al. 2013). Likely due to this multiplicity of phenomena requiring parametrization, stable conditions also pose special challenges to numerical weather prediction (NWP) models. Planetary boundary-layer (PBL) schemes, the turbulence closures employed in NWP models, are more successful during daytime when convection is the sole dominant process for vertical mixing within the boundary layer (Xie et al. 2012). Typical night-time conditions, under stable stratification when convection does not play a role, are not as well reproduced with these PBL schemes (Holtslag et al. 2013).

Large-eddy simulations (LES) avoid the use of PBL schemes by using grid resolutions fine enough to resolve the most energetic eddies (Deardorff 1980), but this is also more challenging with a stable atmosphere. As stability increases, the scale and magnitude of turbulent fluctuations are diminished and finer meshes are required to resolve the dominant turbulent motions (Pope 2000). As computational power grows to meet this challenge, LES is becoming more common in atmospheric studies over complex terrain.

Employing microscale LES to formulate mesoscale parametrizations is a stated goal of the Mountain Terrain Atmospheric Modelling and Observations (MATERHORN) program (Fernando et al. 2015). This Office of Naval Research Multidisciplinary University Research Initiative sponsored field campaigns near Granite Peak, at Dugway Proving Ground in Utah, USA (Figs. 1 and 2). Among the phenomena observed were significant oscillations in the time series of near-surface temperature (e.g. Fig. 3) on the slopes of Granite Peak during all quiescent nights of the MATERHORN's autumn campaign (Lehner et al. 2015; Jeglum et al. 2017). Due to the large magnitude of these oscillations (several °C), displacement of the cold-air pool in the neighbouring basin was hypothesized to be important to these oscillations. Jeglum et al. (2017) provided a more complete description of what they call large temperature fluctuations in the MATERHORN data (Jeglum et al. 2017). Their study also presents some evidence of lee vortices (Epifanio 2003) as the mechanism for the cold-air pool displacement, but observational data to support this are limited even with the project's extensive network of sensors. To bridge the gap in the observations, Jeglum et al. (2017) also simulate the lee vortices in the WRF model with a horizontal grid size, $\Delta x = 500\,\text{m}$, that requires using a PBL turbulence closure. Because the scale of the lee vortices, $\mathcal{O}(1\,\text{km})$, is near the Nyquist limit of these simulations, the features are arguably underresolved. Considering the challenges faced by both observations and previous modelling efforts, an opportunity is presented for LES, the focus of the present study.

Beyond addressing specific questions raised by the MATERHORN field campaign, further development of the LES technique is motivated by many active fields of research. These include those concerned with boundary-layer dynamics, air quality, and weather forecasting. A much discussed case study at the intersection of these fields is the cold-air pool that often persists around Salt Lake City, Utah. Though larger in scale than the cold-air pool investigated here, the Salt Lake Valley cold-air pool is subject to similar climatology and much of the fundamental dynamics are universal to cold-air pools of all scales. The Salt Lake Valley case brings to light issues brought by insufficient resolution that the mesoscale modelling community faces (Lareau et al. 2013). Particularly under stable conditions and in the presence of terrain, which require fine grids to resolve large gradients in temperature and in surface characteristics, respectively, LES can provide added benefits.

We begin with a brief background (Sect. 2) on the fundamental physical processes of interest: cold-air pools, large temperature fluctuations, and lee vortices. We then describe the utilized observational data and detail the configuration of the numerical model. Based on our

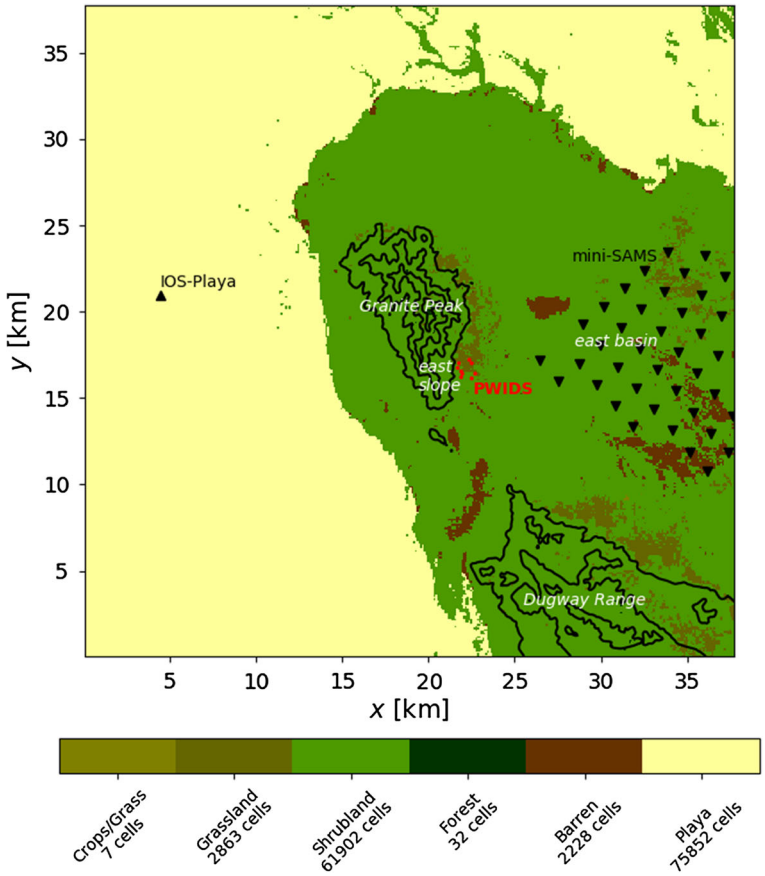

Fig. 1 Large-eddy-simulation domain, d03, with polygons marking the locations of the observation stations used in the current study and white text labels on select geographical areas. The launch site of the radiosonde at IOS-Playa: black, upward-pointed triangle; portable weather instrumentation data systems (PWIDS) on the east slope: red points; 'mini' Surface Atmospheric Measurement Systems (mini-SAMS) array in the east basin: black, downward-pointed triangle. Pixel colours represent categories in the improved land-cover data added to the WRF simulation. Topography contour lines have 200-m intervals

experience configuring the LES model, we propose a new constraint on the timestep related to steep slopes for terrain-following coordinate systems (Sect. 3). We also discuss the model sensitivity to soil moisture initialization and the choice of meteorological forcing (Sect. 4). Simulation results demonstrate the relationship between lee vortices and large temperature fluctuations. The structure of the lee vortices, shown in the potential temperature and vorticity fields, and its comparison to similar idealized models of lee vortices, are also discussed (Sect. 5).

2 Background

Nocturnal cold-air pools develop readily under synoptically quiescent conditions in the sheltered confines of valleys and basins. They are characterized by increased stability and

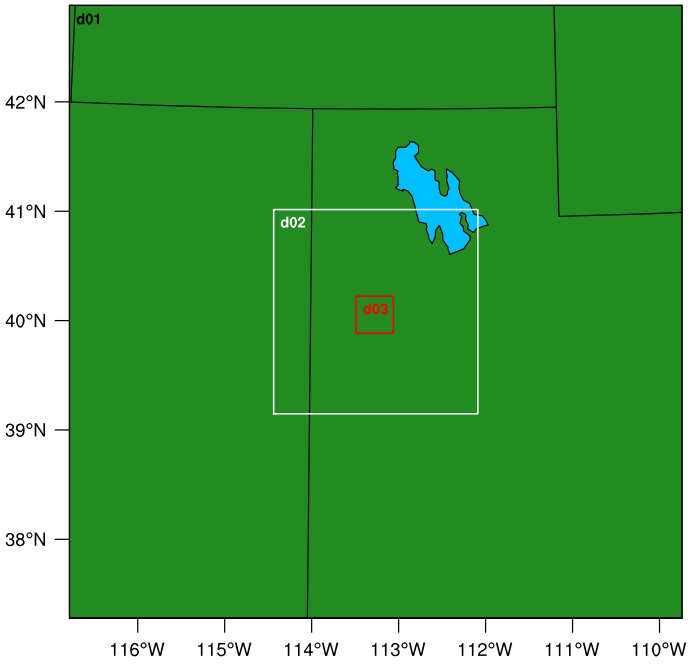

Fig. 2 Nested domains, d02 and d03, shown in the area covered by d01, the outermost parent domain including the Great Salt Lake in the geographical 'chimney' of Utah state (black lines are state boundaries)

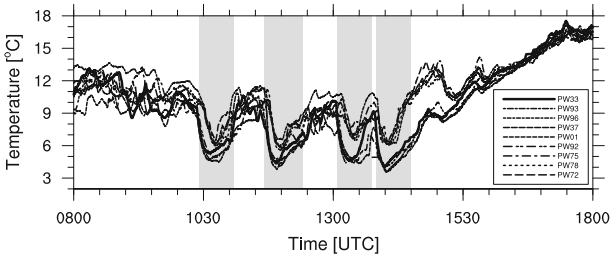

Fig. 3 2-m temperature at the portable weather instrumentation data systems (PWIDS) on the east slope of Granite Peak on 14 October. Locations of the PWIDS are indicated by the red dots in Figure 1. Shading indicates periods of observed large temperature fluctuations

stagnation in the near-surface air. Figure 4 reveals such a cold-air pool in the basin east of Granite Peak, labelled east basin in Fig. 1. The formation of a cold-air pool is ultimately due to the diurnal variation of the surface radiation and energy budget as well as the presence of topography. At night, longwave emission becomes the largest term in the radiation and energy balance, driving the cooling of the near-surface air, which leads to the development of a near-surface stable layer. The deepening of the cold-air pool is the result of radiative and turbulent heat exchange processes, including intermittent shear-induced turbulence at the top of the stable layer (Whiteman et al. 2009). This in situ cooling occurs over flat terrain as well, but lower near-surface temperatures may persist if there is sheltering by topography, which reduces the mixing. Additionally, along the sloped sidewalls, the cooling of near-surface air leads to buoyancy-driven drainage flows. These drainage flows converge in topographic

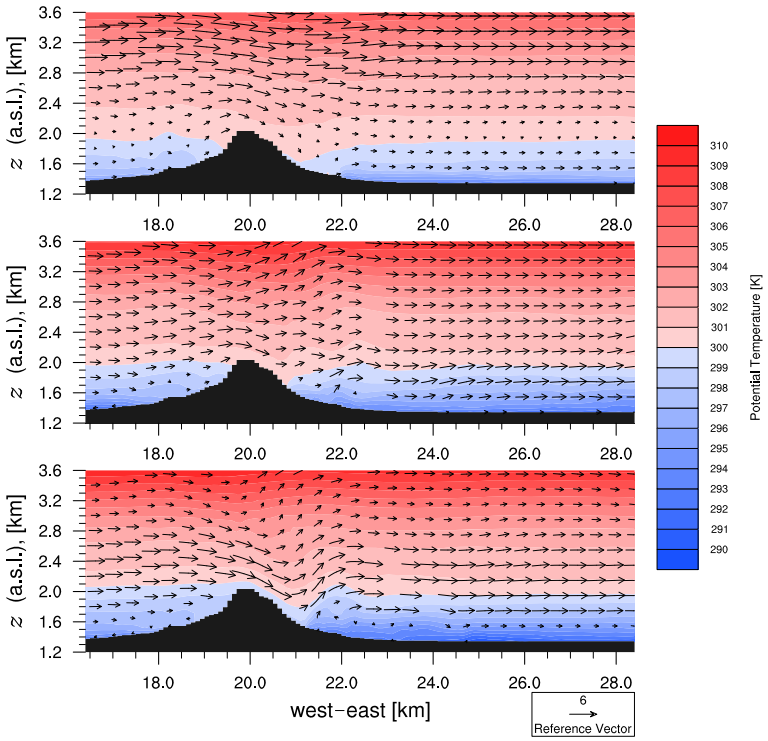

Fig. 4 Potential temperature contours and quiver plots (U–W) from a west–east slice through the middle of d03 and intersecting Granite Peak in 60%-NAM d03, top: 0930 UTC (0330 MDT), middle: 1200 UTC (0600 MDT), bottom: 1330 UTC (0730 MDT)

depressions of all scales, bringing cold-air parcels down the sidewalls to the valley floor or to a point of neutral buoyancy within an extant cold-air pool. This effect is referred to as dynamical cooling (Zardi and Whiteman 2013). Though their relative contributions change throughout the night, the total induced cooling is of comparable magnitude for both in situ and dynamic effects (Burns and Chemel 2014). The temperature anomaly within a cold-air pool could be so significant that a displacement of the cold-air pool would register large changes in temperature at the surface, e.g. along the slope of the basin sidewalls.

In the context of the MATERHORN project, Jeglum et al. (2017) define a large temperature fluctuation as a decrease of at least 3 K within 30 min followed by a recovery of at least 50% of this temperature loss within another hour from the time of minimum temperature. Such a definition effectively isolates large temperature fluctuations associated with displacements of the cold-air pool from fluctuations due to other phenomena such as passing air fronts. The identified large temperature fluctuations are centred on the portion of the slope over which the boundary of the cold-air pool ascends and descends as it is displaced. The study of Jeglum et al. (2017) concluded that the main mechanism for displacing the cold-air pool was an orographic wake similar to those found in the simulations of Epifanio and Rotunno (2005).

From earlier simulations with free slip boundary conditions, Smolarkiewicz and Rotunno (1989) showed that boundary-layer separation is not the impetus for certain wakes in flows with upstream blocking (Fig. 5). In these cases, horizontal vorticity is generated baroclin-

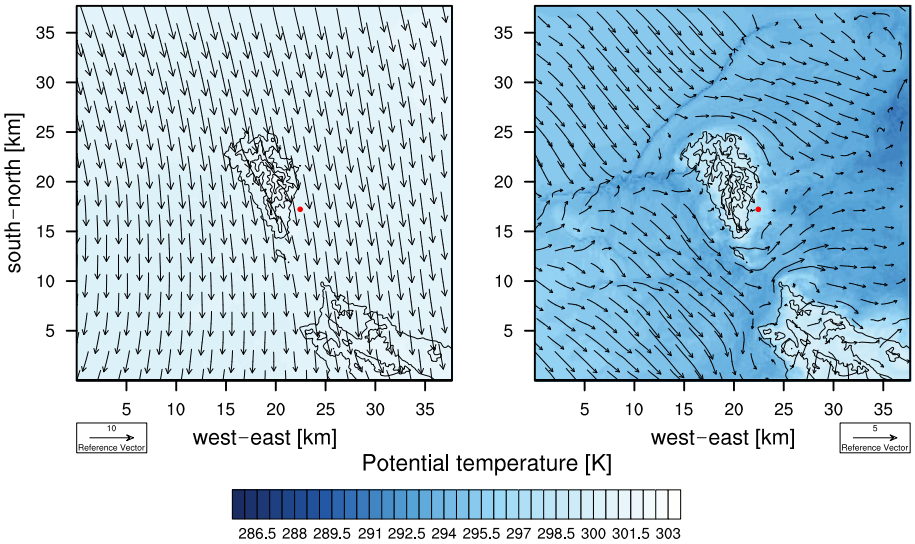

Fig. 5 Potential temperature filled contours and quiver plot of horizontal velocity from 60%-NAM d03. Left panel: At 885 m a.g.l., north-north-westerly flow aloft passes over the mountain. Right panel: At 28 m a.g.l., north-westerly flow is blocked but lee vortices have not yet formed. Both panels from 0930 UTC. Topography contour lines have 200-m intervals. Red dot marks the location of PWIDS 33

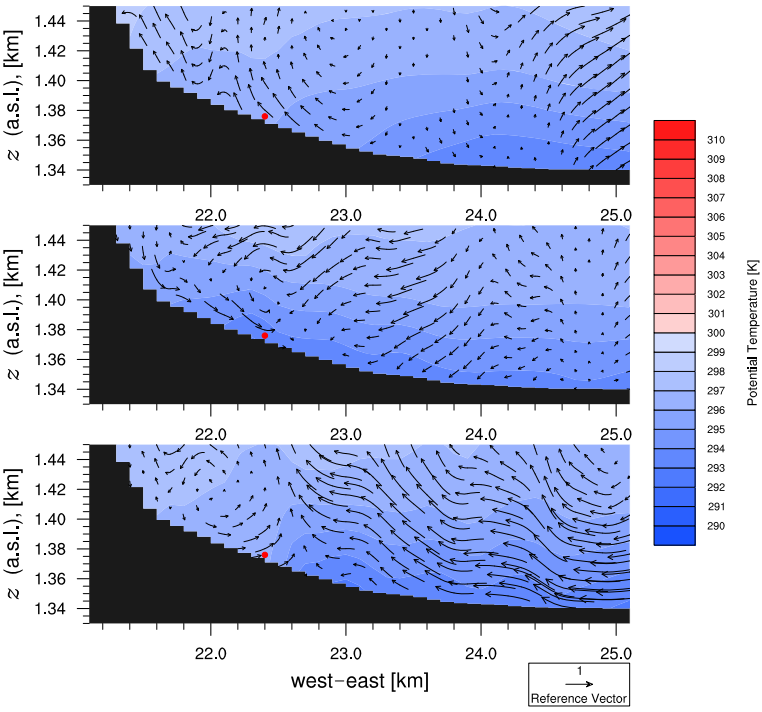

Fig. 6 Potential temperature contours and quiver plots (U–W) from a west–east slice through PWIDS 33 in 60%-NAM d03. Top: 0950 UTC (0350 MDT), middle: 1020 UTC (0420 MDT), bottom: 1050 UTC (0450 MDT)

ically rather than by friction between the terrain and adjacent airstream. As such, these wakes are not dependent on boundary-layer separation like the wakes of classic bluff body theory. Though wakes whose dynamics are dominated by boundary-layer separation can be found in the atmosphere, they are unlikely to occur in the ranges of the controlling non-dimensional parameters, defined below, investigated in the current work (Epifanio 2003). The baroclinicity can be attributed to the deformation of isentropes by the terrain. On the windward slope, Fig. 4 shows the prerequisite 'bulging' of isentropes, and on the lee slope, isentropes are deformed by flow over the obstacle, which is termed the descending flow (Fig. 4). It is important to distinguish between the descending flow and the drainage flow. Drainage flows are the shallow, buoyancy-driven flows that contribute to cold-air pooling in valleys and basins. Descending flows are on the scale of the obstacle and exist even for neutral flows to conserve mass. In certain stratified flow regimes, the descending flow may result in a horizontal potential temperature gradient (Fig. 6). Given a nearly vertical pressure gradient in atmospheric flows, which are approximately hydrostatic, a horizontal component of the potential temperature gradient results in baroclinic generation of horizontal vorticity. This vorticity can be greatly enhanced by the presence of finite amplitude effects resembling hydraulic jumps, i.e., standing density current waves, that might form in the lee of the obstacle (Schär and Smith 1993; Schär and Durran 1997). Ultimately, these processes generate two counter-rotating vertical-axis circulations downwind of the obstacle, which are referred to as lee vortices (Epifanio and Durran 2002a, b).

Work cited above considers obstacles with idealized topography and further simplify the problem by using one or two layers with constant stratification and uniform freestream velocity, as in towing tank experiments, e.g. Baines (1979). A relevant parameter, the non-dimensional mountain height (inverse Froude number), is well defined in the ideal problem,

$$\epsilon = \frac{Nh}{U}, \tag{1}$$

where N is the buoyancy frequency, h is the height of the mountain, and U is the freestream velocity. The horizontal aspect ratio, β, taken as the cross-stream width of the mountain over the along-stream length, is also relevant to this three-dimensional problem in which fluid flows both over and around an obstacle. Given a value of β, there is a critical ϵ above which we expect lee vortices to form. Though the value of this lower bound is determined by the specific geometry in question, for symmetrical and slightly elongated ($\beta \gtrsim 1$) ridges, $\epsilon \approx 1$. Additionally, for the baroclinic mechanism to dominate the wake dynamics, an upper bound is given as $\epsilon \lesssim 10$ based on ideal simulations. At Granite Peak, the mountain geometry gives $\beta \approx 1$, so a moderate value for non-dimensional mountain height, $\epsilon = \mathcal{O}(1)$, suggests lee vortices would form by the baroclinic generation mechanism (Epifanio 2003).

Our study extends the work of idealized simulations of orographic wakes with upstream blocking by including meteorological forcing as well as realistic topography and heterogeneous surface and soil properties. A consequence of the realistic topography is the formation of a cold-air pool in the east basin. The displacement up the slope of this cold-air pool by lee vortices in the wake produces large temperature fluctuations. Additionally, we are able to analyze model skill by comparing our real model to observational data and test the sensitivity to soil moisture and large-scale forcing data.

Table 1 Information on nested simulation domains

Domain	$\Delta x = \Delta y$	$\Delta z_{\min}$–$\Delta z_{\max}$	$Nx \cdot Ny \cdot Nz$	dt[s]	Closure
01	6.3 km	57 m–170 m	100·100·121	30	MYJ
02	2.1 km	57 m–170 m	100·100·121	10	MYJ
03	100 m	57 m–170 m	379·379·121	0.2	TKE 1.5

3 Methods

3.1 Field Observations

The vast observational network available from the MATERHORN field experiment includes sensors of the Granite Mountain Atmospheric Science Testbed (GMAST), and heavily instrumented intensive observing sites (IOS), described in detail in Fernando et al. (2015). Here, we mainly use three observational assets labelled in Fig. 1. We compare our model results with the upstream soundings from IOS-Playa. We also use the 'mini' Surface Atmospheric Measurement Systems (mini-SAMS) array located in the basin east of Granite Peak (east basin) to determine the strength of the nocturnal cold-air pool. Thirdly, a subset of portable weather instrumentation data systems (PWIDS) deployed near IOS-ES on the eastern slope of Granite Peak (east slope) record the large temperature fluctuations observed during intensive observation period 6 (IOP) on 14 October 2012.

3.2 Nested WRF Models

The simulations presented here were performed with the Weather Research and Forecasting (WRF) model developed by the National Center for Atmospheric Research (NCAR), version 3.7.1 (Skamarock et al. 2008). The dynamic core of the model provides a numerical solution of the compressible flow equations with a third-order Runge–Kutta time advancement scheme, with split time stepping to handle acoustic modes, as well as fifth-order horizontal advection and third-order vertical advection.

Physical parametrizations employed in the simulations include the Noah land-surface model (Chen and Dudhia 2001), the Rapid Radiative Transfer Model for longwave radiation (Mlawer et al. 1997), the Dudhia shortwave radiation model (Dudhia 1989), and a surface-layer parametrization based on Monin–Obukhov similarity theory (Chen et al. 1997). Following Massey et al. (2014), a 'hybrid' soil thermal conductivity scheme is implemented in the WRF model to correct the tendency for this model to underpredict the diurnal temperature range. 'Hybrid' refers to the use of two forms of parametrizations: those of Johansen (1975) are used for all soil classes except silt loam and sandy loam, which are handled by another scheme proposed by McCumber and Pielke (1981).

Figure 2 illustrates the nested domain set-up, while Table 1 provides additional information on each domain in the nest. Domains 1 and 2 resemble typical domains used in mesoscale NWP and use a PBL scheme for their turbulence closure (Janjić 1994). Domain 3 is run at large-eddy permitting resolution. Specifically, 100 m horizontal grid spacing and vertical grid spacing between 57 and 170 m are used. Using a staggered grid, the model's first half level where horizontal velocities are computed is approximately 28 m above ground level (a.g.l.). This near-surface vertical resolution is necessarily quite coarse due to the stability constraint related to resolving steep slopes, as further discussed below, but still allows a reasonable

Table 2 Information on model configurations used in the tests of sensitivity to soil moisture and meteorological forcing

Name	Forcing source	Forcing resolution	Soil moisture
Min-NAM	NAM	12 km	All layer volumetric water content set to 0.005 m^3 m^{-3} everywhere but lakes
60%-NAM	NAM	12 km	5 cm volumetric water content set to 60% of NAM values everywhere but lakes
Full-NAM	NAM	12 km	Unaltered NAM values
60%-GFS	GFS	0.5°	5 cm volumetric water content set to 60% of GFS values everywhere but lakes
Full-GFS	GFS	0.5°	Unaltered GFS values

representation of the lee vortices. For this finest resolved domain we use a turbulent kinetic energy (TKE) 1.5-order LES turbulence closure, appropriate at higher resolutions (Deardorff 1980; Wyngaard 2004).

All domains are initialized with meteorological data either from the Global Forecast System (GFS) or from the North American Mesoscale (NAM) model reanalysis, made publicly available by the National Oceanic and Atmospheric Administration (NOAA). Both models are from the National Center for Environmental Protection (NCEP) but differ in horizontal resolution, GFS at 0.5 ° (∼ 50 km) and NAM at a finer 12 km. The model is initialized at 0000 UTC 14 October 2012, 1800 local time (MDT) 13 October 2012. Model initialization precedes IOP 6 of the MATERHORN autumn campaign by 8 h for model spin-up, which is excluded from the analysis. The GFS or NAM data provide the lateral boundary conditions for the coarsest grid throughout the duration of the simulation. For the nested domains, lateral boundary conditions are provided through a one-way nesting procedure.

3.3 Land Cover and Topography

Of the land-cover data provided by NCAR for ready use with the WRF model, the finest available resolution is 30 arcsec, which is about 1 km at middle latitudes. Our simulations use a higher resolution land cover dataset created for 4DWX, an operational model used by Army forecasters at Dugway Proving Ground (Liu et al. 2008). These data are resolved at 1 arcsec and contain additional land-cover types: lava, playa, and white sand.

Similarly, standard topography data available with the WRF model are at resolutions no higher than 30 arcsec. Because the LES domain is much finer, we implement the United States Geological Survey (USGS) National Elevation Dataset (Gesch et al. 2002) topography with a resolution of 1/3 arcsec, roughly 10 m at these latitudes, for the LES domain.

3.4 Soil Moisture Initialization

The initialization of soil moisture is varied to test model sensitivity and to correct a bias in near-surface temperatures (Massey et al. 2014). Higher model soil moisture results in higher soil conductivity and heat capacity. The resulting increase in soil heat storage leads to model

daytime cold biases and night-time warm biases (Zhang et al. 2013; Massey et al. 2016). To mitigate these errors, the 50-mm soil moisture is initialized to 60% of the values provided by the forcing dataset for two simulations, 60%-NAM and 60%-GFS. The sensitivity study also includes simulations with unaltered soil moisture, Full-NAM and Full-GFS, and with soil moisture further reduced to the minimum allowed by the WRF model, the Min-NAM simulation (Table 2).

3.5 Timestep and Vertical Resolution Limits

One of the challenges with fine horizontal resolution over complex terrain is that the resolved slopes become steeper with increasing grid resolution, and can lead to numerical stability issues that are limiting, potentially prohibitive. To address this, the mesoscale simulations and the LES must differ in the relationship between horizontal grid size and timestep. From Table 1, note the two larger domains conform to the rule-of-thumb Courant limit developed for mesoscale simulations in the WRF model,

$$\Delta t \lesssim C \Delta x^*, \tag{2}$$

with Δt being the larger, non-acoustic timestep, $C = 6\,\mathrm{s\,km^{-1}}$ and Δx^* taken as the smallest horizontal grid spacing. In the more finely resolved LES, the timestep suggested by this rule of thumb, $\Delta t = 0.6\,\mathrm{s}$, and a slightly reduced timestep, $\Delta t = 0.4\,\mathrm{s}$, lead to the LES terminating due to numerical instability almost immediately after initialization. Greatly reducing the timestep through trial and error to $\Delta t = 0.2\,\mathrm{s}$ was required for model stability. This more restrictive timestep limit can be explained by modifying the Courant limit with another stability limit that follows from the work of Mahrer (1984) on the use of a terrain-following coordinate system over steep terrain,

$$\tan\alpha < b\frac{\Delta z}{\Delta x}, \tag{3}$$

for maximum slope α over a grid spacing of Δx and typically $1 \leq b \lesssim 5$ (Poulos 1996; Zhong and Chow 2013).

We hypothesize that the Mahrer condition must be combined with the Courant limit for cases in which the distance between a near-surface grid point and the sloped boundary in the true horizontal directions is less than the grid spacing. With this assumption, we take $\Delta x^* = \Delta z / \tan\alpha$ as a more restrictive length scale in the Courant condition,

$$\Delta t \lesssim C\frac{\Delta z}{\tan\alpha}, \tag{4}$$

and substitute (3), the inequality constraint on $\tan\alpha$,

$$C \cdot \frac{\Delta z}{b\frac{\Delta z}{\Delta x}} \lesssim C\frac{\Delta z}{\tan\alpha}, \tag{5}$$

to propose a new rule-of-thumb for timestep selection over steep slopes which ensures meeting the requirements of both the Courant condition and the steep terrain condition,

$$\Delta t \lesssim \frac{C}{b}\Delta x \lesssim C\frac{\Delta z}{\tan\alpha}. \tag{6}$$

The second inequality simply restates the steep terrain condition while the first inequality of (6) is a new condition that takes the same form as the WRF model's original rule-of-thumb

Table 3 Mini-SAMS 2-m temperature biases calculated for various time intervals: pre-sunrise, post-sunrise, and the whole morning of IOP 6

Simulation	Bias (RMSE) [K] $0800 < t < 1340$ UTC	Bias (RMSE) [K] $1340 < t < 1800$ UTC	Bias (RMSE) [K] $0800 < t < 1800$ UTC
Full-GFS d03	6.59 (6.61)	1.50 (2.60)	4.35 (5.24)
Full-NAM d03	5.47 (5.48)	1.01 (2.18)	3.50 (4.35)
60%-NAM d03	3.03 (3.07)	0.82 (1.25)	2.05 (2.43)
Min-NAM d03	1.70 (1.77)	−0.20 (0.78)	0.86 (1.42)

Courant condition: direct proportionality between timestep and horizontal grid spacing, now with a smaller coefficient, C/b, as $b \geq 1$.

Using this new condition, the timestep chosen by trial-and-error, $\Delta t = 0.2\,\text{s}$, implies a value of $b \approx 3$ which is typical for this coefficient. Further, our attempts to refine vertical resolution lead to model degradation, likely due to the violation of the second inequality, the steep terrain limit. Maximum resolved slopes are $\alpha \approx 45°$, such that vertical refinement is limited by

$$\Delta z \gtrsim \tan\alpha \frac{\Delta x}{b} \approx (1)\frac{100}{3} = 33.3\ , \tag{7}$$

with Δz in m, which roughly matches the height of our first half model level, 28 m a.g.l., where horizontal velocities are computed. As such, the vertical resolutions used in the current simulations are necessarily coarse to ensure stability. The variable vertical spacing is determined through the WRF model's default grid stretching procedure upon specifying 121 vertical levels and retaining the default model top at approximately 500 hPa.

4 Model Validation and Sensitivity Tests

4.1 Sensitivity to Soil Moisture

Figure 7 compares radiosonde observations of potential temperature, wind direction, and wind speed to those from the large-eddy simulations of Min-NAM, 60%-NAM, and Full-NAM simulations. The radiosondes released from IOS-Playa, marked in Fig. 1, on 14 October at 0850 UTC (0250 MDT) and 1203 UTC (0603 MDT) are upstream of Granite Peak during the time period in which large temperature fluctuations are observed on the east slope. Except for the minimal soil moisture simulation, Min-NAM, the first one or two grid points in the WRF model exhibit the expected nocturnal warm bias. Over the next several grid points above ground level, the model shows a cold bias. Such a 'smoothed' temperature profile supports the hypothesis that 2-m temperature positive biases are due to an overly dissipative parametrization of the nocturnal boundary layer. The Min-NAM simulation exhibits an atypical nocturnal cold bias at the lowest model levels, indicating an overcorrection of soil moisture. Further aloft, differences between simulations with varied soil moisture initializations vanish and the WRF models, regardless of soil moisture, compare similarly well to the observation soundings above the first few grid levels.

Turning to instruments downstream of the mountain in the east basin containing the cold-air pool, Fig. 8 shows time series of 2-m temperature biases averaged over the 40 mini-SAMS stations within the LES domain of the Min-NAM, 60%-NAM, Full-NAM, and

Full-GFS simulations. In the east basin, the WRF model's near-surface temperature bias remains positive, i.e. a warm bias, until some time after sunrise (1340 UTC or 0740 MDT). During these hours before sunrise, simulations with increasing soil volumetric water content show increasingly warm biases. Unaltered GFS soil moisture produces the worst errors (Table 3). In the east basin, even the model with the driest soil has this characteristic warm bias, unlike the first grid level at the radiosonde site. The presence of the nocturnal warm bias in the east basin, even with minimal soil moisture as in the Min-NAM simulation, is likely due to a combination of excess mixing in the stable boundary layer and a lack of cold-air inflow by drainage flows. Jeglum et al. (2017) also reported a nocturnal warm bias in their simulations with coarser horizontal resolution (500 m) even though they were able to use finer vertical resolution due to more moderate terrain slopes at this resolution.

Dynamic cooling is entirely absent because drainage flows are too shallow to be resolved in the current simulations (Smith and Porté-Agel 2014). Further, as stability inhibits the mixing

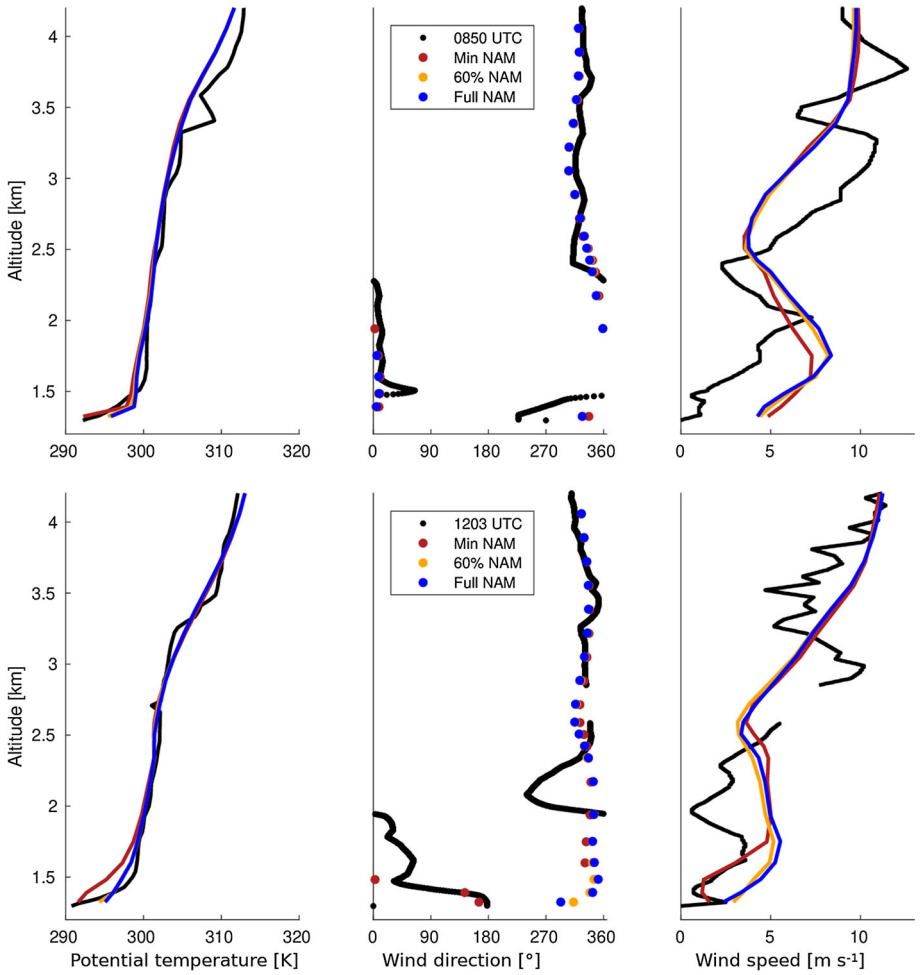

Fig. 7 Soundings released at 0850 and 1203 UTC from the radiosonde station marked IOS-Playa in Fig. 1 compared to the large-eddy simulations, Min-NAM d03, 60%-NAM d03, and Full-NAM d03

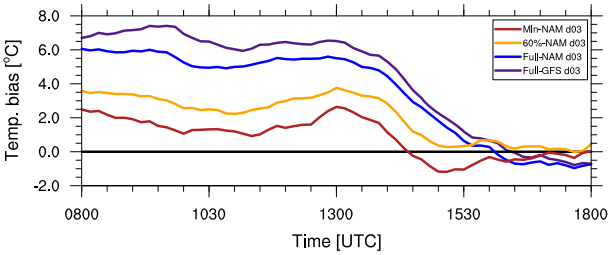

Fig. 8 Biases of 2-m temperature, calculated as modelled minus observed temperature averaged over 40 mini-SAMS weather stations in the east basin, comparing the large-eddy simulations (d03) of the Min-NAM, 60%-NAM, Full-NAM, and Full-GFS simulations

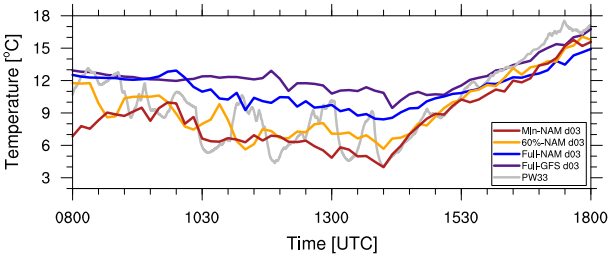

Fig. 9 2-m temperature from PWIDS 33 on the east slope of Granite Peak, comparing large-eddy simulations forced by NAM with full, 60%, and minimal soil moisture initializations as well as the full soil moisture LES forced by GFS

Table 4 East slope PWIDS 2-m temperature biases calculated for various time intervals: pre-sunrise, post-sunrise, and the whole morning of IOP 6

Simulation	Bias (RMSE) [K] $0800 < t < 1340$ UTC	Bias (RMSE) [K] $1340 < t < 1800$ UTC	Bias (RMSE) [K] $0800 < t < 1800$ UTC
Full-NAM d03	1.84 (2.31)	−0.52 (1.48)	0.81 (2.00)
60%-NAM d03	−0.44 (1.65)	−0.89 (1.17)	−0.62 (1.46)
Min-NAM d03	−1.85 (2.34)	−1.65 (1.83)	−1.74 (2.11)
Full-GFS d03	2.74 (3.19)	0.72 (1.64)	1.84 (2.62)
60%-GFS d03	1.13 (2.11)	−0.73 (1.32)	0.32 (1.82)

of potentially warmer air aloft, this exacerbates the long-standing modelling challenge of maintaining a strongly stable near-surface inversion. Considering the condition in Eq. 6, vertical resolutions fine enough to resolve the drainage flows, $\mathcal{O}(1\ \text{m})$, lead to numerical instabilities in a terrain-following coordinate system over slopes as steep as those of Granite Peak, at least for current horizontal resolutions. Recent advances with the immersed boundary method may help resolve this issue in the future (Arthur et al. 2018; Bao et al. 2018; Wiersema et al. 2018). (For example, Arthur et al. (2018) simulated drainage flows on Granite Peak in a semi-idealized set-up with 25-m horizontal resolution.) Until these numerical techniques are available, shallow drainage flows in steep terrain will remain a challenge for NWP models. Without this dynamic cooling, nocturnal warm biases can be expected in areas of cold-air pooling even when minimizing soil moisture to tune the in situ cooling.

Figure 9 shows time series of 2-m temperature from one east slope PWIDS station, PWIDS 33, against spatially interpolated data from the WRF model with various initial soil moisture fields. For the same LES models, Table 4 gives 2-m temperature biases averaged over all nine PWIDS (only eight when PWIDS 37 is missing data) on the east slope of Granite Peak. The biases are further averaged over different time periods. Though the Full-GFS simulation performs best after the morning transition, the full soil moisture simulations have the largest errors during the period of large temperature fluctuations at night when they show strong warm biases. The Min-NAM simulation exhibits an atypical nocturnal cold bias, again indicating an overcorrection of soil moisture. The simulation initialized with 60% soil moisture appears to be a good compromise, with a mean bias less than 0.5 K during the pre-sunrise period (Table 4). The simulations initialized with 60% soil moisture are selected for the comparison of meteorological forcing and the discussion of dynamics in the following sections.

4.2 Sensitivity to Meteorological Forcing Data

Two meteorological forecast products are chosen to initialize all domains and to force d01, the outermost mesoscale domain, by providing lateral boundary conditions. Though commonly used, the relatively coarse GFS resolution (0.5 °) may not suffice over complex terrain where topographically-forced flows are expected. To address this concern, the other forecast product, the finer resolved (12 km) NAM model, provides finer resolved forcing data in the current simulations. However, neither the NAM-forced nor GFS-forced LES produce large temperature fluctuations when initialized with full soil moisture fields (Fig. 9), i.e. for Full-NAM and Full-GFS simulations, so the attention of this section narrows to models initialized with 60% soil moisture, 60%-NAM and 60%-GFS simulations.

Figure 10 compares potential temperature, wind direction, and wind speed from the radiosondes to those from d03 of 60%-GFS and of 60%-NAM simulations. The radiosondes released from IOS-Playa, marked in Fig. 1, on 14 October at 0850 UTC (0250 MDT) and 1203 UTC (0603 MDT) are upstream of Granite Peak during the time period in which large temperature fluctuations are observed on the east slope. At the lowest grid level, potential temperature does not differ between the models as much as in the soil sensitivity tests. Both models show a near-surface inversion that is weaker than in the observations partly due to a near-surface warm bias. Wind direction between models and observations agree above ridge height, ≈2.3 km above sea level (a.s.l.). Below this height, differences are apparent, particularly at the lowest levels. This disagreement may result from differences in the extent of blocking between the modelled and physical flows. Wind speed agreement is good on average, but the observations show high wavenumber oscillations that neither model resolves.

Turning to instruments downstream of the mountain in the east basin containing the cold-air pool, Fig. 11 shows 2-m temperature biases averaged over the 40 mini-SAMS stations within the LES domain. NAM-forced simulations slightly outperform those forced by GFS but all models exhibit a persistent nocturnal warm bias despite the soil moisture correction. In the late morning, some time after sunrise (1340 UTC or 0740 MDT), both mesoscale simulations remain too warm though with greatly reduced magnitudes compared to biases before sunrise. At the same time, LES model biases decrease to nearly zero in the east basin.

In the time series of 2-m temperature on the east slope of Granite Peak shown in Fig. 12, 60%-NAM d03 and the 60%-GFS d03 show more appreciable differences than in the upstream radiosonde soundings or in the average temperature bias across the mini-SAMS array. Further, these disparities have greater importance in this study motivated by the signature of large temperature fluctuations in these time series. The mesoscale simulations, 60%-NAM

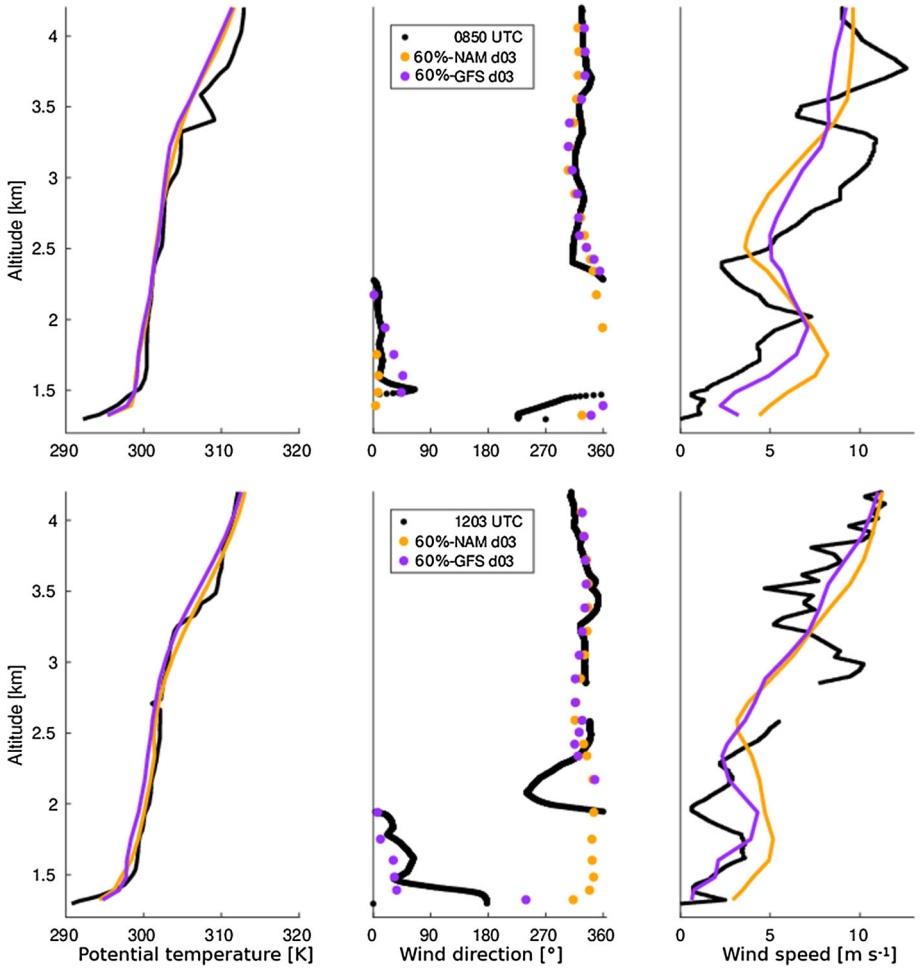

Fig. 10 Soundings released at 0850 (top) and 1203 UTC (bottom) from the radiosonde station marked IOS-Playa on Fig. 1 compared to the large-eddy simulations, 60%-NAM d03 and 60%-GFS d03

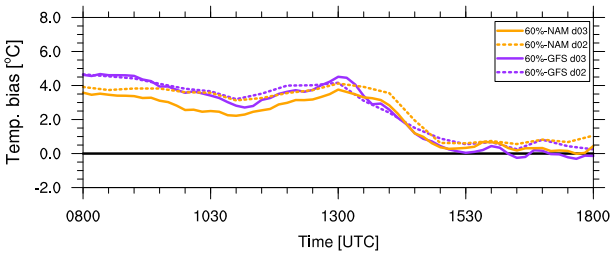

Fig. 11 Biases of 2-m temperature, calculated as modelled minus observed temperature averaged over 40 mini-SAMS weather stations in the east basin, comparing the finer mesoscale simulation (d02) and the large-eddy simulation (d03) from NAM and GFS both with the 60% soil moisture initialization

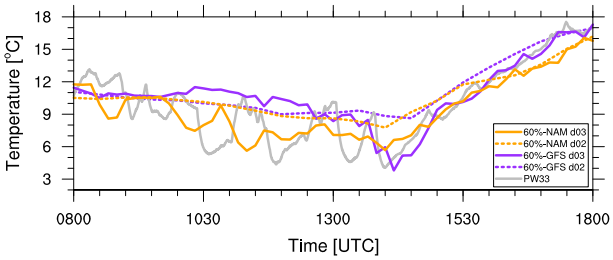

Fig. 12 2-m temperature from a PWIDS station on the east slope of Granite Peak, comparing the finer mesoscale simulation (d02) and the large-eddy simulation (d03) from NAM and GFS both with the 60% soil moisture initialization

d02 and 60%-GFS d02, contain no large temperature fluctuations and the 60%-GFS d03 LES only resolves one large temperature fluctuation. Interestingly, the timing of the sole large temperature fluctuation reproduced by 60%-GFS d03 is nearly perfect. However the study of this large temperature fluctuation, the latest, is complicated by the fact that recovery of temperature occurs after sunrise (1340 UTC or 0740 MDT) such that any warming cannot be fully attributed to the recession of the cold-air pool. Two large temperature fluctuations occur in 60%-NAM d03, but they are not precisely concurrent with the observed temperature fluctuations. Even with errors predicting the timing, 60%-NAM d03 has the lowest magnitude bias during the early morning period between 0800 and 1340 UTC (0200 and 0740 MDT, Table 4). As such, 60%-NAM d03 seems to capture the phenomenon of large temperature fluctuations best, and results from this configuration will be the focus of the following sections.

5 Results and Discussion

5.1 Modelled Large Temperature Fluctuations

Four observed large temperature fluctuations are highlighted grey in Fig. 3, the time series of 2-m temperature from nine PWIDS on the east slope of Granite Peak. The first two of these, recorded at all PWIDS on the east slope, are roughly concurrent with two large temperature fluctuations in the LES, d03, of the 60%-NAM simulation (Fig. 12). To analyze the occurrence of multiple large temperature fluctuations within the same model, we focus on 60%-NAM d03 during the period of large fluctuations roughly concurrent with the two in the observation data.

In 60%-NAM d03, a large temperature fluctuation begins at 0950 UTC (0350 MDT). Temperatures decrease by 3 K to a first temperature minimum at 1020 UTC (0420 MDT), until recovering most of the temperature loss by 1050 UTC (0450 MDT). Immediately following this temperature recovery, another large temperature fluctuation is initiated and the temperature decreases by just over 4 K by 1120 UTC (0520 MDT). This time, the temperature does not fully recover and rises only 2 K by 1140 UTC (0540 MDT). During these times, the occurrence of large temperature fluctuations in the LES reduces the temperature on the east slope of Granite Peak in comparison to its parent mesoscale model, which does not resolve any large fluctuations (Fig. 12).

Though 60%-NAM d03 resolves large temperature fluctuations, the temperature minima remain several K higher than the minima from field data. This is due to the nocturnal warm

bias in the basin to the east of the Granite Peak, which remains positive even with minimal soil moisture (Fig. 8). When insufficiently cold basin air is displaced up the mountain slope to the location of PWIDS 33 in the LES model, a smaller temperature decrease is recorded than when colder basin air is displaced up the mountain in reality.

5.2 Cold-Air Pool Displacement by Lee Vortices

Flow visualizations are presented as evidence of lee vortices being the mechanism for the cold-air pool displacement. The instances of large temperature fluctuations in the model time series coincide with the existence of vertical axis circulations with a return flow that advects air from the east basin to the east slope.

Figure 5 shows the state of the horizontal flow and temperature fields from the first half model level at 28 m a.g.l. from 60%-NAM d03 at 0930 UTC (0330 MDT), immediately before a large temperature fluctuation is initiated. We see the flow aloft is north–north–westerly (left panel), as in the radiosondes, such that lee vortices would form near the stations on the east slope of Granite Peak. Inspection of lower level flow at this time shows that the flow is blocked, though no lee vortices are present before the model large temperature fluctuation initiates (right panel). By 0940 UTC (0340 MDT), lee vortices have begun to form with a return flow that advects colder air from the east basin cold-air pool toward the east slope stations (Fig. 13). Temperature there continues to decrease over the next half hour while the return flow is present. Then, the centres of the circulations are advected downstream and temperature on the east slope begins to recover at 1020 UTC (0420 MDT) as the zonal component of the wind switches from easterly to westerly (Fig. 14). During these times, another feature of lee vortices becomes visible. These are the 'warm cores' of the lee vortices predicted by ideal simulations (Schär and Durran 1997).

During the interim of the two largest model temperature fluctuations, PWIDS 33 occupies the boundary of colder (darker blue) air to the east and warmer (lighter blue) air upslope to the west (Fig. 15). The lee vortices are being advected farther downstream while simultaneously growing in size. Eventually, a second large temperature fluctuation is initiated by these same lee vortices, now large enough for the return flow to reach the east slope stations yet again. Similar to the previous fluctuation, temperature decreases while the return flow is present. Unlike the previous large temperature fluctuation, the second recovery in temperature is not associated with advection of the circulations farther from the observation station. Instead, through the gap between Granite Peak and the Dugway Range to the south, flows are growing in strength until they eventually 'wash out' the lee vortices (Fig. 16).

From this series of events, we see that multiple large temperature fluctuations can be associated with the same lee vortices that have changed size or position relative to the observation site. While noting a single pair of lee vortices may be associated with multiple large temperature fluctuations, it is also worth noting that there may be lee vortices without any large temperature fluctuations. This is the case in Full-NAM d03: lee vortices occur (Fig. 17), but no *large* temperature fluctuation is recorded on the east slope. Though Full-NAM d03 shows fluctuations in temperature at the same time 60%-NAM d03 does, the magnitude of the fluctuation is diminished due to the increased warm bias in the cold-air pool. As the temperature decrease is less than 3 K, this event does not qualify as a large temperature fluctuation by the threshold values defined by Jeglum et al. (2017) though it is dynamically similar in that lee vortices are associated with some fluctuations in temperature on the lee slope.

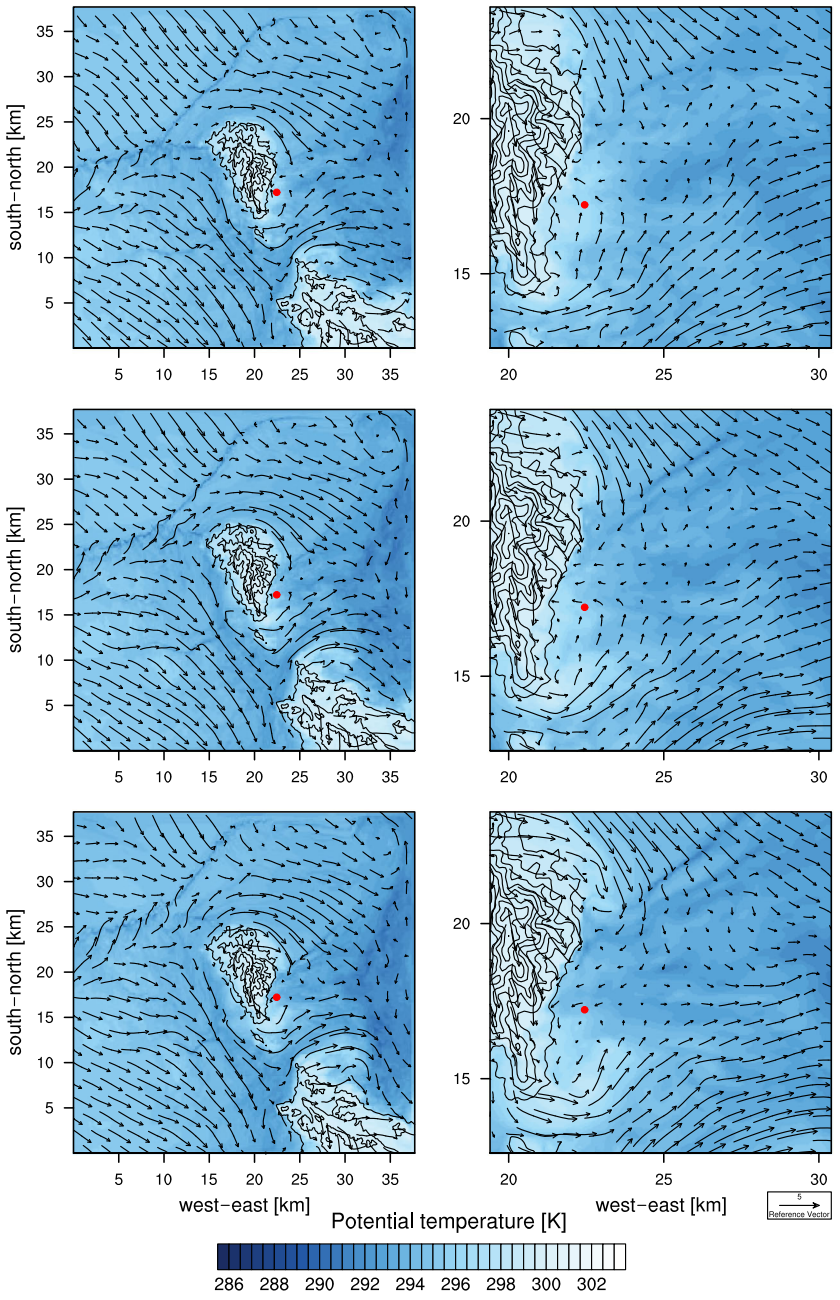

Fig. 13 Contours of potential temperature and quiver plot of horizontal velocity at 28 m a.g.l. from 60%-NAM d03. Topography contour lines have (left) and 100 m (right) intervals, respectively. Left and right panels are taken from the same times; the left panel shows the full extent of d03, and the right panels is zoomed in around the east slope and east basin. Top panels at 0940 UTC. Middle panels at 0950 UTC. Bottom panels at 1000 UTC. Flow remains blocked, lee vortices with return flow correspond with a decrease in temperature on the east slope during the first model large temperature fluctuation discussed in the body text

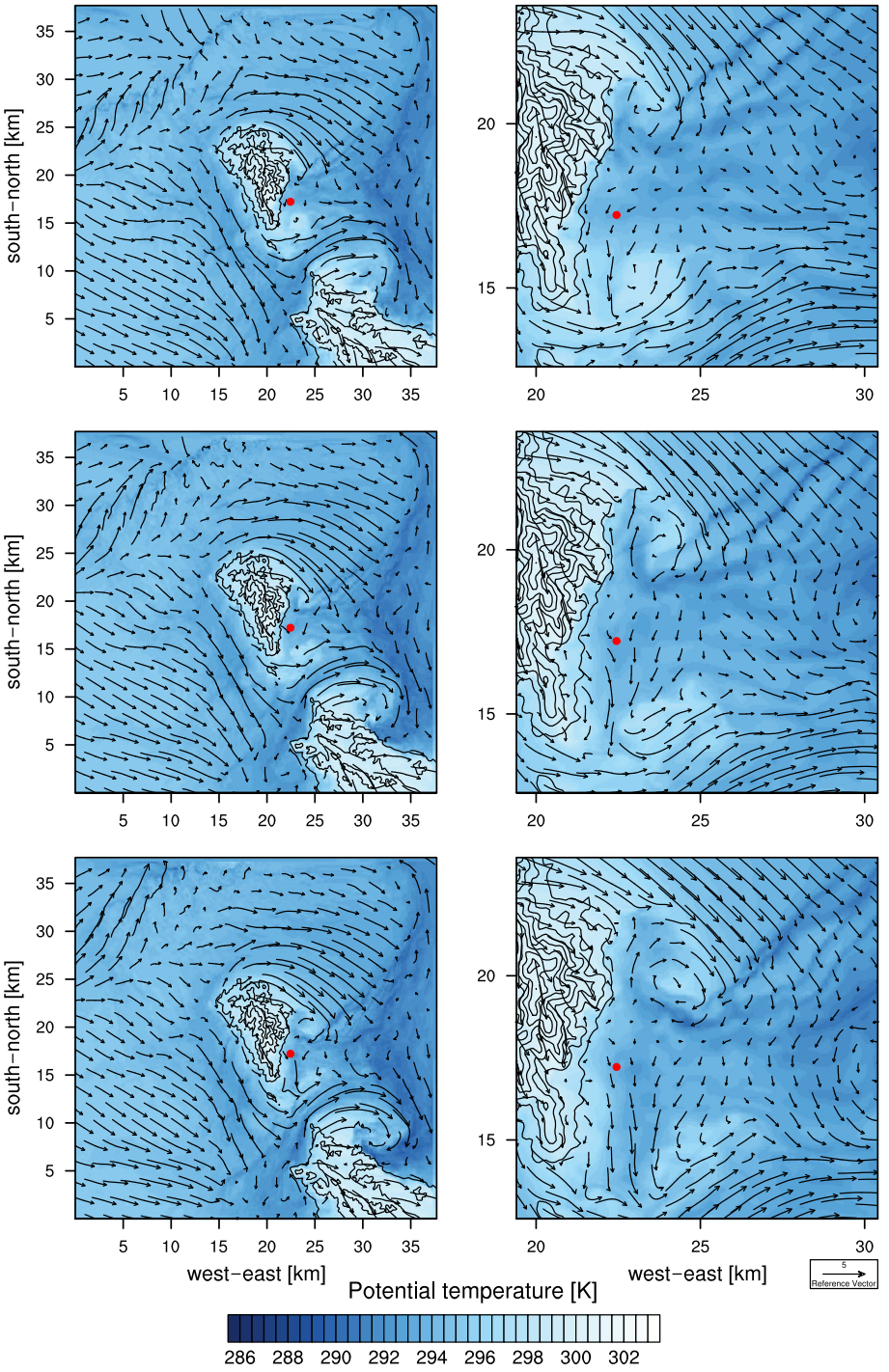

Fig. 14 As in Fig. 13 but for 1010 UTC (top), 1020 UTC (middle), and 1030 UTC (bottom). Lee vortices are advected downstream, ceasing the decreasing in temperature on the east slope during the first model large temperature fluctuation discussed in the body text

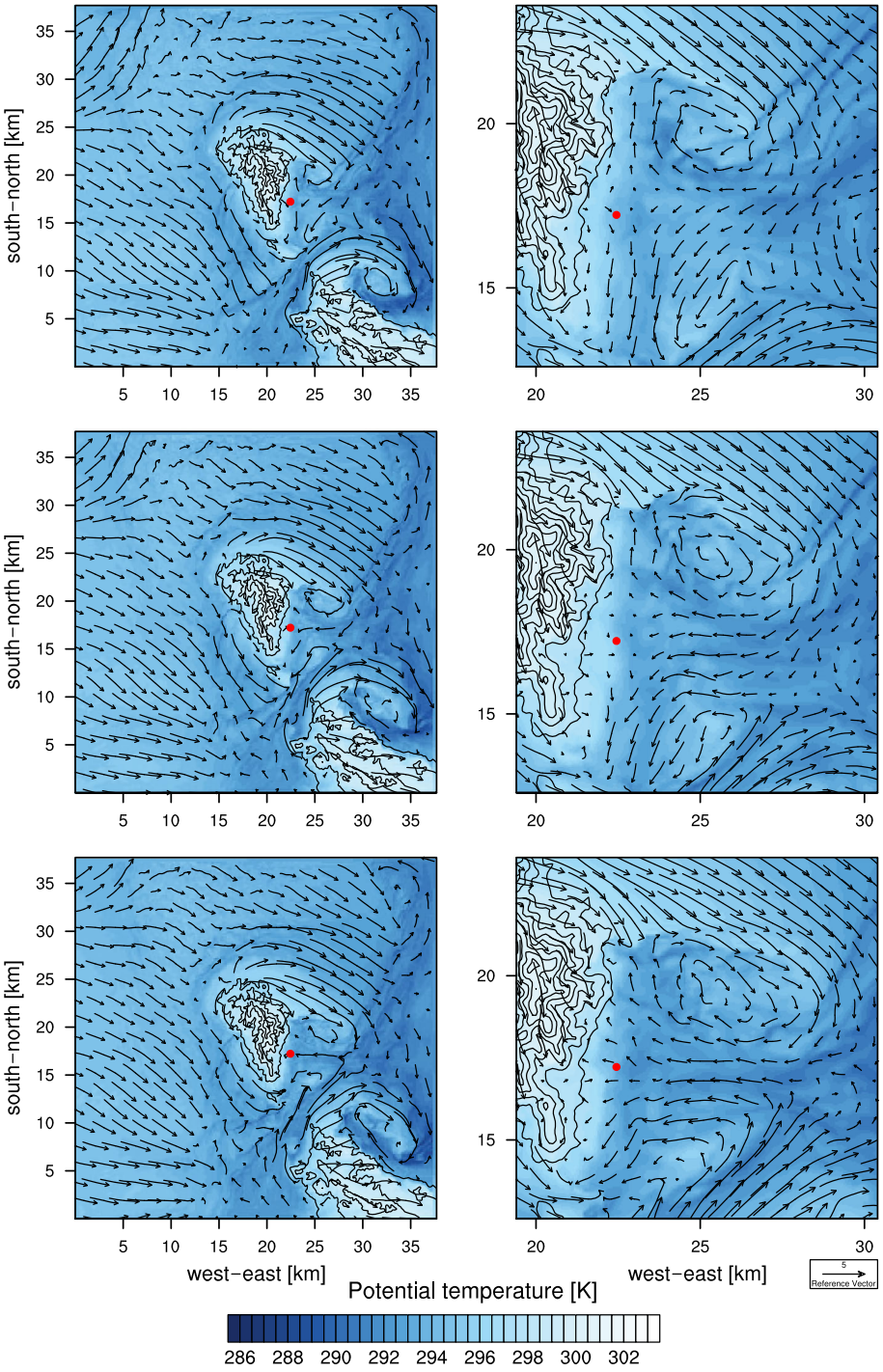

Fig. 15 As in Fig. 13 but for 1040 UTC (top), 1050 UTC (middle), and 1100 UTC (bottom). Lee vortices grow as they are advected downstream, eventually return flow reaches the east slope initiating the second model large temperature fluctuation discussed in the body text

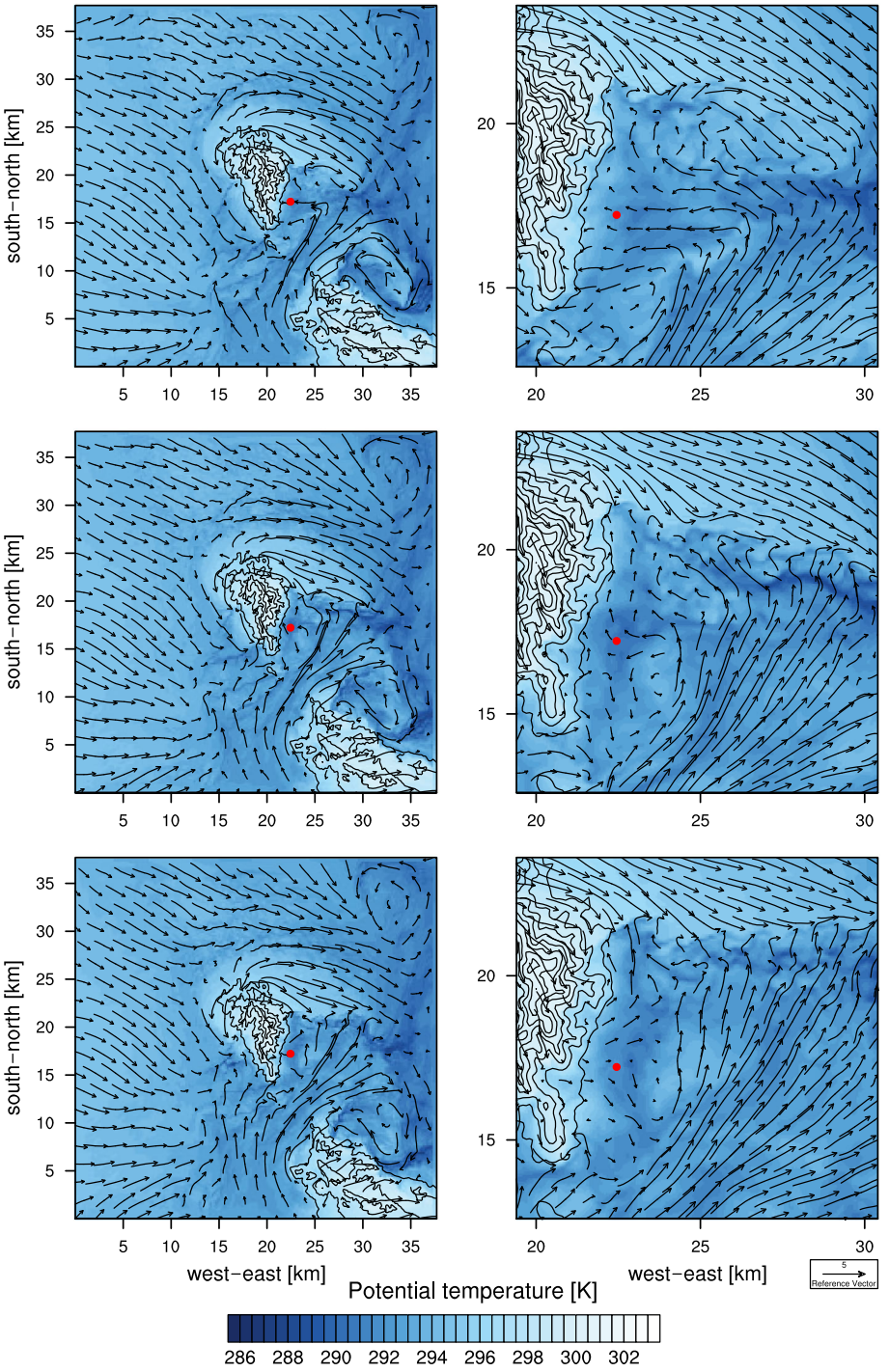

Fig. 16 As in Fig. 13 but for 1110 UTC (top), 1120 UTC (middle), and 1130 UTC (bottom). Return flow continues the temperature decrease on the east slope until a strong gap flow disrupts the lee vortex circulation, ending the second model large temperature fluctuation discussed in the body text

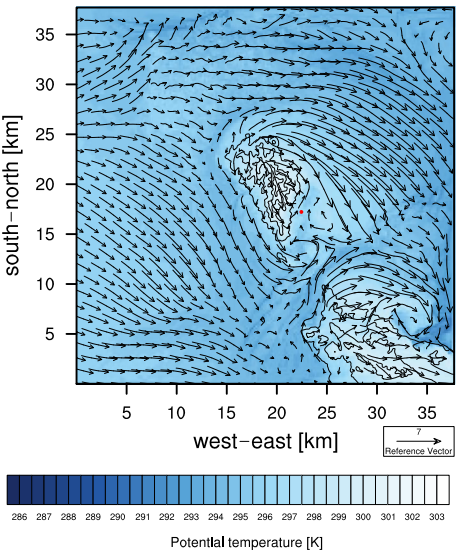

Fig. 17 Contours of potential temperature and quiver plot of horizontal velocity at 28 m a.g.l. from Full-NAM d03. Taken at 1100 UTC (0500 MDT). Topography contour lines have 200-m intervals. Lee vortices dynamics are similar to the 60%-NAM d03 despite the lack of large temperature fluctuations. Two counter-rotating vertical axis circulations are visible near the east slope

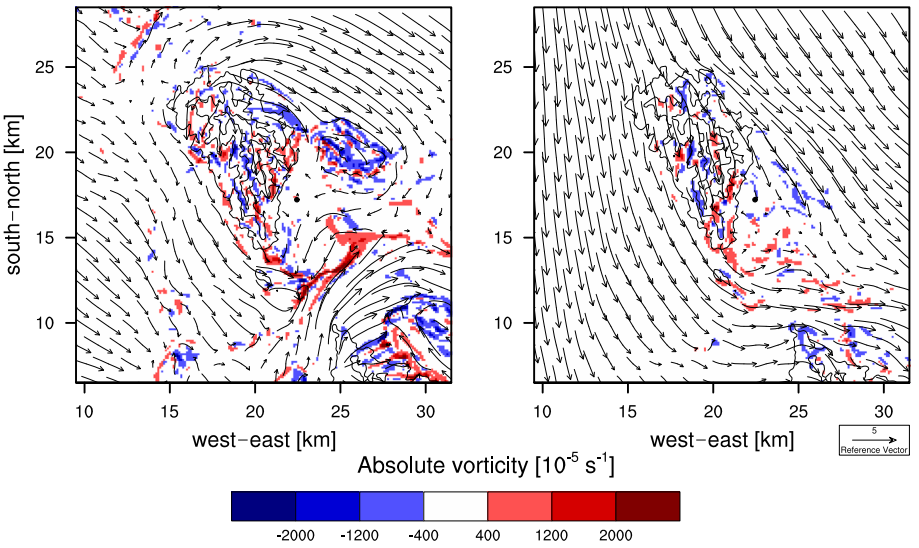

Fig. 18 Vorticity contours at 1050 UTC (0450 MDT) from 60%-NAM d03. Left: First model level, 28 m a.g.l., with vorticity pattern of lee vortices that agrees qualitatively with those of Fig. 1b in Epifanio and Durran (2002b) from idealized simulations. Right: Third model level, 200 m a.g.l. Topography contour lines have 200-m intervals

5.3 Vortical Structure

Two counter-rotating vertical axis circulations develop on the lee side of Granite Peak in our real case large-eddy simulations. Though the baroclinicity generates horizontal vorticity, tilting of the horizontal vorticity in turn generates vertical vorticity whose spatial distribution can be compared to that of ideal simulations, e.g. those of Epifanio and Durran (2002a). In Fig. 18, we see the blocked northwesterly wind diverted around the northern lateral edge

of Granite Peak flows into a region of negative (clockwise) vertical vorticity, while flow diverted around the southern edge leads to a region of positive vertical vorticity. The sign of vorticity matches that expected from idealized simulations, as seen in Fig. 1b in Epifanio and Durran (2002b). The vorticity pattern is stronger at the lowest model level, 28 m a.g.l. shown in the left panel, and extends approximately 200 m a.g.l. until it is nearly absent at the third model level shown in the right panel. Unlike idealized simulations of similar phenomena, vorticity is already present in the inflow but is also clearly enhanced on the lee side of Granite Peak. It is unclear how much of this enhancement is associated with further generation of vorticity by the baroclinic generation mechanism of Smolarkiewicz and Rotunno (1989), or with the interactions with the hydraulic-jump-like lee wave discussed by Schär and Smith (1993). An analysis following Epifanio and Durran (2002b) would be necessary to partition lee side vorticity among these mechanisms but is not conducted here. Rather, it suffices to demonstrate that the combination of these effects generates sufficient lee side vorticity to induce the reversed flow necessary for large temperature fluctuations to occur.

Contours of potential temperature from vertical cross-sections provide evidence for two of the proposed vorticity generation mechanisms, baroclinicity and finite-amplitude effects. In Fig. 4, a mountain lee wave is present through most of the night. Within a hydraulic-jump-like region of the lee wave, vertical vorticity is generated by the tilting and stretching of vortex tubes. Some amount of this vorticity originates from the baroclinic generation mechanism. Baroclinicity on the lee slope is also evident in the potential temperature field. Far from the obstacle, isentropes are nearly horizontal but over the lee slope, they are tilted downward due to the potentially warmer descending flow. As such, there exists a significant horizontal component of the potential temperature gradient (Fig. 6). From hydrostatic balance, the pressure gradient is nearly vertical such that a horizontal ($-x$ direction in the $x-z$ planes plotted here) potential temperature gradient generates horizontal (directed into the page) vorticity baroclinically, as in the classic 'lock exchange' hydraulics problem.

5.4 Upstream Conditions

Though the orographic wakes presented here resemble those previously studied by analytical means or idealized simulations, e.g. those of Smolarkiewicz and Rotunno (1989), Schär and Durran (1997), and Epifanio and Rotunno (2005), there are important extensions and additional complications to consider in the real case LES of the current study. Beyond the complex shape of the terrain, nonuniform upstream conditions pose such a challenge. As mentioned previously, the presence of vorticity upstream of Granite Peak is one deviation from the ideal inflow conditions. Similarly, the inflow is nonuniform for wind speed, wind direction and buoyancy frequency.

Profiles of wind direction from the model in Fig. 7 or by comparing the vector plots in Fig. 5, we see the low-level free stream flow is west–north–westerly while flow farther aloft is north–north–westerly. In this case, the directional shear has the same sign as expected from an Ekman spiral, a common feature of stably stratified boundary layers in rotating reference frames. Further study would benefit from revisiting the idealized simulations while imposing directionally sheared inflow to better identify the impact of such nonuniform velocity profiles.

Similar to the wind conditions in the real case models, the background stratification is neither uniform nor steady as it is in idealized models. Rather, potential temperature has a more realistic profile in which stratification is stronger near the cold ground. Epifanio and Rotunno (2005) used a two layer background stratification profile with this feature, but within each layer the simplification to constant stratification is still applied. In that study, the

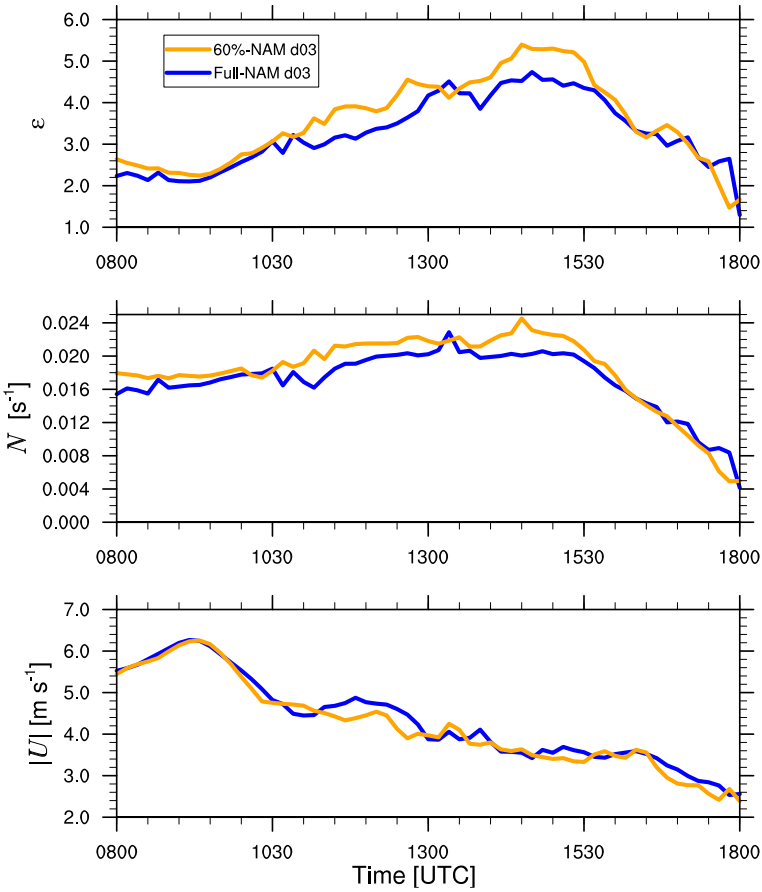

Fig. 19 Time series of non-dimensional mountain height, $\epsilon = Nh/U$ (top), computed with mountain height, h, taken as 800 m; buoyancy frequency, N (middle), taken as average over first five grid levels; and wind speed, $|U|$ (bottom), taken as average over first 10 grid levels at 40°12.5' N, 113°22.5' W in the LES forced by NAM with full or 60% soil moisture initialization

characteristic buoyancy frequency used in the non-dimensional mountain height is that of the lower and more strongly stratified layer; we follow this approach below.

5.5 Non-dimensional Parameter Space

As a practical matter, the heterogeneity of buoyancy frequency, N, and of wind speed, U, preclude an unambiguous definition of non-dimensional mountain height, $\epsilon = Nh/U$. Nonetheless, ad hoc methods can be developed to calculate ϵ with bulk lapse rates and average velocities. Using the first five grid levels to compute a characteristic buoyancy frequency, and the first 10 grid levels for a characteristic velocity scale, we calculate ϵ at a point north–east of Granite Peak chosen a posteriori on the basis of the vector plots. The peak height at Granite Peak is 840 m above the valley floor (Fernando et al. 2015). We use a rounded $h = 800$ m to calculate non-dimensional mountain height plotted in the top panel of Fig. 19. The variability of ϵ is decomposed into N and U, shown in the other panels. Though buoyancy

frequency is generally increasing throughout the night, most of the increase in ϵ is due to a decrease in wind speed during this time. Soon after sunrise (1340 UTC), non-dimensional mountain height begins to rapidly decrease despite low wind speeds. At this time, changes in ϵ are dominated by the decrease of N as the nocturnal boundary layer is broken up.

Together with the horizontal aspect ratio, the non-dimensional mountain height determines the regime of orographic wake formation in the idealized problem. The time series of ϵ in Fig. 19 reveals an average value of approximately 3 throughout the period of lee vortex formation in 60%-NAM d03. Though Granite Peak is elongated in the longitudinal direction, consideration of the skewed angle of approach of the low-level impinging flow justifies taking $\beta \approx 1$, i.e. the cross-stream and along-stream dimensions of the obstacle are approximately equal. These values of β and ϵ lie within the regime of blocked flow and baroclinic generation of lee vortices in the parameter space of the idealized problem (see Epifanio 2003 for a schematic of this parameter space). That is, ϵ is not so large that boundary-layer separation, rather than baroclinicity, is likely to dominate the wake dynamics as it might for $\epsilon \gtrsim 10$ (Epifanio 2003). This suggests that the same non-dimensional parameters may prove valuable in the analysis of real case lee vortex dynamics and in the ultimate parametrization of these orographic wakes in large scale models. Though a large enough non-dimensional mountain height seems a necessary condition for lee vortex formation, it is not sufficient. Lack of lee vortices in the later half of the early morning is due to a strong gap flow to the south of Granite Peak that interferes with dynamics of the orographic wake in 60%-NAM d03.

In the full soil moisture simulations, values for non-dimensional mountain height also lie within the lee vortex regime of the $\beta - \epsilon$ parameter space and we see lee vortices develop (Fig. 17). Though there is a return flow in the wake, there are no large temperature fluctuations at the location of the east slope stations in the full soil moisture LES (Fig. 9). This lack of large temperature fluctuations in the full soil moisture simulation is explained by the east basin warm bias that is much worse in the full soil moisture simulations (Fig. 8). Only when both a cold-air pool that is sufficiently cold and lee vortices are present, as in 60%-NAM d03, do large temperature fluctuations occur.

6 Summary and Conclusions

Nested large-eddy simulations using the WRF model are shown here to be able to recreate the unique large temperature fluctuations observed on the east slope of Granite Peak during IOP 6 of the MATERHORN field campaign. The LES results and analysis presented are able to explain the topography-induced lee vortices that generate these temperature fluctuations in concert with displacement of the east basin cold pool. This success required careful attention to surface conditions and numerical parameters such as grid spacing and timestep considerations over steep terrain. The ubiquity of these temperature fluctuations, occurring on all quiescent nights of the MATERHORN's autumn campaign, suggests that these constitute a significant source of mesoscale model error. Temperature-sensitive operations located on sloped terrain, e.g. fire weather prediction, could therefore benefit from the utilization of large-eddy simulations to supplement and extend traditional forecast products.

Along the eastern slope of Granite Peak, the large temperature fluctuations are associated with the displacement of a cold-air pool that forms in the nearby basin. The warm bias of the model cold-air pool is greatly improved by drying the shallowest layer and thus increasing in situ cooling. Numerical stability constraints limit the vertical grid spacing allowed with the fine horizontal (100 m) resolution used here and the associated steep terrain slopes, which

affects the model's ability to resolve drainage flows. Without this dynamical cooling from drainage flows, a warm bias remains in the east basin and diminishes the temperature decrease on the slope when the cold-air pool is displaced upslope. Future studies may avoid this source of error by using a vertical grid that is not terrain-following, such as the immersed-boundary method (Lundquist et al. 2012; Arthur et al. 2018; Bao et al. 2018; Wiersema et al. 2018), to enable better representation of flow near the terrain surface.

A new stability limit was also proposed here to enable simulations over steep terrain: reducing the constant of proportionality between timestep and grid spacing by a factor of $b \approx 3$ in the current work or, more generally, $1 \leq b \lesssim 5$ (Poulos 1996; Zhong and Chow 2013). Future studies that continue to use terrain-following coordinate systems over steep slopes should consider this new stability limit as a guideline in selecting numerical simulation parameters.

We have shown that the cold-air pool displacement is associated with the return flow of the lee vortices, as postulated by Jeglum et al. (2017) and shown in their WRF model simulations for another date. These lee vortices occur in the real case simulation within a non-dimensional parameter regime that agrees well with the regime in which lee vortices are expected to form in idealized simulations, such as those of Smolarkiewicz and Rotunno (1989) and Epifanio and Rotunno (2005). However, due to the interference of other flow phenomena like gap flows, large non-dimensional mountain height is not a sufficient condition to predict the occurrence of lee vortices. As such, the parametrization of lee vortices for mesoscale and larger scale models cannot be completed without simultaneously addressing a wider range of interactions between stable flows and complex terrain.

Acknowledgements The MATERHORN Program was funded by the Office of Naval Research MURI Award N00014-11-1-0709 (Program Officers: Drs. Ronald Ferek and Daniel Eleuterio), with additional funding from the Army Research Office (Program Officers: Gordon Videen and Walter Bach), Air Force Weather Agency, Research Offices of University of Notre Dame and University of Utah, and Wayne and Diana Murdy Family Endowment at Notre Dame. We thank the MATERHORN field team and Dugway Proving Ground staff. Simulations were performed on the UC Berkeley Savio computing cluster.

References

Arthur RS, Lundquist KA, Mirocha JD, Chow FK (2018) Topographic effects on radiation in the WRF model with the immersed boundary method: implementation, validation, and application to complex terrain. Mon Weather Rev 146(10):3277–3292

Baines P (1979) Observations of stratified flow past three-dimensional barriers. J Geophys Res Oceans 84(C12):7834–7838

Baines PG (1998) Topographic effects in stratified flows. Cambridge University Press, Cambridge

Bao J, Chow FK, Lundquist KA (2018) Large-eddy simulation over complex terrain using an improved immersed boundary method in the weather research and forecasting model. Mon Weather Rev 146(9):2781–2797. https://doi.org/10.1175/MWR-D-18-0067.1

Burns P, Chemel C (2014) Evolution of cold-air-pooling processes in complex terrain. Boundary-Layer Meteorol 150(3):423–447. https://doi.org/10.1007/s10546-013-9885-z

Chen F, Dudhia J (2001) Coupling an advanced land surface-hydrology model with the Penn State-NCAR MM5 modeling system. Part I: model implementation and sensitivity. Mon Weather Rev 129(4):569–585

Chen F, Janjić Z, Mitchell K (1997) Impact of atmospheric surface-layer parameterizations in the new land-surface scheme of the NCEP mesoscale eta model. Boundary-Layer Meteorol 85(3):391–421

Chow FK, De Wekker SF, Snyder BJ (2013) Mountain weather research and forecasting: recent progress and current challenges. Springer, New York

Deardorff JW (1980) Stratocumulus-capped mixed layers derived from a three-dimensional model. Boundary-Layer Meteorol 18(4):495–527

Dudhia J (1989) Numerical study of convection observed during the winter monsoon experiment using a mesoscale two-dimensional model. J Atmos Sci 46(20):3077–3107

Epifanio CC (2003) Lee vortices. In: Holton JR, Pyle J, Curry JA (eds) Encyclopedia of atmospheric sciences. Elsevier, Amsterdam, pp 1150–1160
Epifanio C, Durran D (2002a) Lee-vortex formation in free-slip stratified flow over ridges. Part I: comparison of weakly nonlinear inviscid theory and fully nonlinear viscous simulations. J Atmos Sci 59(7):1153–1165
Epifanio C, Durran D (2002b) Lee-vortex formation in free-slip stratified flow over ridges. Part II: mechanisms of vorticity and PV production in nonlinear viscous wakes. J Atmos Sci 59(7):1166–1181
Epifanio CC, Rotunno R (2005) The dynamics of orographic wake formation in flows with upstream blocking. J Atmos Sci 62(9):3127–3150
Fernando H, Pardyjak E, Di Sabatino S, Chow F, De Wekker S, Hoch S, Hacker J, Pace J, Pratt T, Pu Z et al (2015) The MATERHORN: unraveling the intricacies of mountain weather. Bull Am Meteorol Soc 96(11):1945–1967
Gesch D, Oimoen M, Greenlee S, Nelson C, Steuck M, Tyler D (2002) The national elevation dataset. Photogramm Eng Remote Sens 68(1):5–32
Holtslag AAM, Svensson G, Baas P, Basu S, Beare B, Beljaars ACM, Bosveld FC, Cuxart J, Lindvall J, Steeneveld GJ, Tjernström M, Van De Wiel BJH (2013) Stable atmospheric boundary layers and diurnal cycles: challenges for weather and climate models. Bull Am Meteorol Soc 94(11):1691–1706. https://doi.org/10.1175/BAMS-D-11-00187.1
Janjić ZI (1994) The step-mountain eta coordinate model: further developments of the convection, viscous sublayer, and turbulence closure schemes. Mon Weather Rev 122(5):927–945
Jeglum M, Hoch S, Jensen D, Dimitrova R, Silver Z (2017) Large temperature fluctuations due to cold air pool displacement along the lee slope of a desert mountain. J Appl Meteorol Clim 56(4):1083–1098
Johansen O (1975) Thermal conductivity of soils. PhD thesis. University of Trondheim, Norway
Lareau NP, Crosman E, Whiteman CD, Horel JD, Hoch SW, Brown WO, Horst TW (2013) The persistent cold-air pool study. Bull Am Meteorol Soc 94(1):51–63
Lehner M, Whiteman CD, Hoch SW, Jensen D, Pardyjak ER, Leo LS, Di Sabatino S, Fernando HJ (2015) A case study of the nocturnal boundary layer evolution on a slope at the foot of a desert mountain. J Appl Meteorol Clim 54(4):732–751
Liu Y, Warner TT, Bowers JF, Carson LP, Chen F, Clough CA, Davis CA, Egeland CH, Halvorson SF, Huck TW Jr et al (2008) The operational mesogamma-scale analysis and forecast system of the US army test and evaluation command. Part I: Overview of the modeling system, the forecast products, and how the products are used. J Appl Meteorol Clim 47(4):1077–1092
Lundquist KA, Chow FK, Lundquist JK (2012) An immersed boundary method enabling large-eddy simulations of flow over complex terrain in the WRF model. Mon Weather Rev 140(12):3936–3955
Mahrer Y (1984) An improved numerical approximation of the horizontal gradients in a terrain-following coordinate system. Mon Weather Rev 112(5):918–922
Massey JD, Steenburgh WJ, Hoch SW, Knievel JC (2014) Sensitivity of near-surface temperature forecasts to soil properties over a sparsely vegetated dryland region. J Appl Meteorol Clim 53(8):1976–1995
Massey JD, Steenburgh WJ, Knievel JC, Cheng WY (2016) Regional soil moisture biases and their influence on WRF model temperature forecasts over the intermountain west. Weather Forecast 31(1):197–216
McCumber MC, Pielke RA (1981) Simulation of the effects of surface fluxes of heat and moisture in a mesoscale numerical model: Part 1. Soil layer. J Geophys Res Oceans 86(C10):9929–9938
Mlawer EJ, Taubman SJ, Brown PD, Iacono MJ, Clough SA (1997) Simulation of the effects of surface fluxes of heat and moisture in a mesoscale numerical model: 1. Soil layer. J Geophys Res Atmos 102(D14):16663–16682
Pope SB (2000) Turbulent flows. Cambridge University Press, Cambridge
Poulos GS (1996) The interaction of katabatic winds and mountain waves. PhD thesis. Colorado State University
Schär C, Durran DR (1997) Vortex formation and vortex shedding in continuously stratified flows past isolated topography. J Atmos Sci 54(4):534–554
Schär C, Smith RB (1993) Shallow-water flow past isolated topography. Part I: vorticity production and wake formation. J Atmos Sci 50(10):1373–1400
Skamarock WC, Klemp JB, Dudhia J, Gill DO, Barker DM, Wang W, Powers JG (2008) A description of the advanced research WRF version 3. NCAR, Tech Rep
Smith CM, Porté-Agel F (2014) An intercomparison of subgrid models for large-eddy simulation of katabatic flows. Q J R Meteorol Soc 140(681):1294–1303
Smolarkiewicz P, Rotunno R (1989) Low Froude-number flow past 3-dimensional obstacles. Part I: baroclinically generated lee vortices. J Atmos Sci 46(8):1154–1164. https://doi.org/10.1175/1520-0469(1989)046<1154:LFNFPT>2.0.CO;2
Whiteman CD, Hoch SW, Poulos GS (2009) Evening temperature rises on valley floors and slopes: their causes and their relationship to the thermally driven wind system. J Appl Meteorol Clim 48(4):776–788

Wiersema D, Lundquist K, Chow F (2018) Development of a multiscale modeling framework for urban simulations in the weather research and forecasting model. Lawrence Livermore National Lab (LLNL), Livermore, CA (United States), Tech Rep

Wyngaard JC (2004) Toward numerical modeling in the "Terra Incognita". J Atmos Sci 61(14):1816–1826

Xie B, Fung JC, Chan A, Lau A (2012) Evaluation of nonlocal and local planetary boundary layer schemes in the WRF model. J Geophys Res Atmos 117(D12)

Zardi D, Whiteman CD (2013) Diurnal mountain wind systems. In: Chow FK, De Wekker SF, Snyder BJ (eds) Mountain weather research and forecasting: recent progress and current challenges. Springer, Netherlands, Dordrecht, pp 35–119

Zhang H, Pu Z, Zhang X (2013) Examination of errors in near-surface temperature and wind from WRF numerical simulations in regions of complex terrain. Weather Forecast 28(3):893–914

Zhong S, Chow FK (2013) Meso- and fine-scale modeling over complex terrain: parameterizations and applications. In: Chow FK, De Wekker SF, Snyder BJ (eds) Mountain weather research and forecasting: recent progress and current challenges. Springer, Netherlands, Dordrecht, pp 591–653